Acta Crystallographica Section D
Biological Crystallography
ISSN 0907-4449

Structural changes caused by radiation-induced reduction and radiolysis: the effect of X-ray absorbed dose in a fungal multicopper oxidase

Eugenio De la Mora,[a] Janet E. Lovett,[b,c,d] Christopher F. Blanford,[e,f] Elspeth F. Garman,[g] Brenda Valderrama[a] and Enrique Rudino-Pinera[a]*

[a]Medicina Molecular y Bioprocesos, Instituto de Biotecnología, Universidad Nacional Autónoma de México, Avenida Universidad 2001, Cuernavaca, Morelos 62210, Mexico, [b]Centre for Advanced Electron Spin Resonance, Inorganic Chemistry Laboratory, University of Oxford, South Parks Road, Oxford OX1 3QR, England, [c]Sir William Dunn School of Pathology, University of Oxford, South Parks Road, Oxford OX1 3RE, England, [d]EaStCHEM School of Chemistry, Joseph Black Building, The King's Buildings, Edinburgh EH9 3JJ, Scotland, [e]Department of Chemistry, Inorganic Chemistry Laboratory, University of Oxford, South Parks Road, Oxford OX1 3QR, England, [f]School of Materials, University of Manchester, Manchester Interdisciplinary Biocentre, 131 Princess Street, Manchester M1 7DN, England, and [g]Laboratory of Molecular Biophysics, Department of Biochemistry, University of Oxford, South Parks Road, Oxford OX1 3QU, England

Correspondence e-mail: rudino@ibt.unam.mx

Received 30 September 2011
Accepted 7 February 2012

PDB References: Cg L, 4a2d; 4a2e; 4a2f; 4a2g; 4a2h.

X-ray radiation induces two main effects at metal centres contained in protein crystals: radiation-induced reduction and radiolysis and a resulting decrease in metal occupancy. In blue multicopper oxidases (BMCOs), the geometry of the active centres and the metal-to-ligand distances change depending on the oxidation states of the Cu atoms, suggesting that these alterations are catalytically relevant to the binding, activation and reduction of O_2. In this work, the X-ray-determined three-dimensional structure of laccase from the basidiomycete *Coriolopsis gallica* (Cg L), a high catalytic potential BMCO, is described. By combining spectroscopic techniques (UV–Vis, EPR and XAS) and X-ray crystallography, structural changes at and around the active copper centres were related to pH and absorbed X-ray dose (energy deposited per unit mass). Depletion of two of the four active Cu atoms as well as low occupancies of the remaining Cu atoms, together with different conformations of the metal centres, were observed at both acidic pH and high absorbed dose, correlating with more reduced states of the active coppers. These observations provide additional evidence to support the role of flexibility of copper sites during O_2 reduction. This study supports previous observations indicating that interpretations regarding redox state and metal coordination need to take radiation effects explicitly into account.

1. Introduction

Dioxygen (O_2) is a ubiquitous terminal acceptor of electrons in biological systems in processes such as cellular respiration. However, O_2 reduction is kinetically slow since one-electron transfer to O_2 is favoured kinetically but is thermodynamically endergonic and also because the two-electron reduction of O_2 (S = 1, triplet) to peroxide (O_2^{2-}) (S = 0, singlet) is spin-forbidden (Kosman, 2010). For this reason, catalysts that can decrease the overpotential (the thermodynamic driving force required to drive an electrochemical reaction from equilibrium) for the four-electron reduction of O_2 (E° = 1.23 V, 298 K) are attracting both theoretical and practical interest (Lewis & Nocera, 2006). Among the metal catalysts normally used in inorganic chemistry, the materials that show the highest activity are based on platinum (Pt; Paulus *et al.*, 2002). However, the high cost of Pt and its undesirable characteristics, such as its substantial overpotential for O_2 and peroxide (O_2^-) production, limit the range of compatible materials and restrict the use of Pt in new applications (Dos Santos *et al.*, 2010). In contrast to Pt-based materials, enzymes such as the blue multicopper oxidases (BMCOs) are efficient catalysts of the O_2-reduction reaction, carrying out fast four-electron

reduction of O_2 to $2H_2O$ at small overpotentials and without releasing reactive intermediates.

BMCOs are present in all kingdoms, with the fungal laccases being the most important group both in number and in extent of characterization. They possess biochemical and electronic properties that make them a very attractive target for biotechnological applications such as bioremediation, biological fuel cells and sensors (Tye *et al.*, 2005; Cracknell *et al.*, 2008; Kunamneni *et al.*, 2008). These enzymes are distinguished from other copper-binding proteins such as azurins, plastocyanins and tyrosinases by the fact that they contain a minimum of four catalytic copper ions classified into three classes according to their spectroscopic properties (Solomon *et al.*, 1996). The type 1 (T1 Cu) or 'blue' copper has an intense $SCys \rightarrow Cu^{II}$ charge-transfer (CT) transition detectable at around 610 nm and is also distinguished by a narrow parallel hyperfine splitting ($A_{\parallel}$ = 40–95 $\times$ 10^{-4} cm^{-1}) in its electron paramagnetic resonance (EPR) spectrum. The type 2 (T2 Cu) or 'normal' copper is characterized by a typical EPR signal with a larger parallel hyperfine splitting ($A_{\parallel}$ = 140–200 $\times$ 10^{-4} cm^{-1}), but is not detectable in the UV–visible region. Finally, the type 3 (T3 Cu) or binuclear copper site is observable as a shoulder on an absorption band at 330 nm and does not typically exhibit an EPR signal owing to the presence of a strongly antiferromagnetic coupled Cu^{II} pair that is hydroxide bridged (Machonkin *et al.*, 2001).

The electrons required for BMCO-catalyzed O_2 reduction are provided by substrate oxidation occurring at the T1 Cu (Solomon *et al.*, 1996). Electrons extracted from substrate molecules are transferred ~13 Å from the T1 Cu to the trinuclear centre (TNC) made up by the binuclear T3 Cu and the mononuclear T2 Cu, where oxygen reduction takes place (Cole *et al.*, 1990). Two acidic residues, which are structurally conserved among all known BMCOs (Quintanar *et al.*, 2005), play a crucial role during O_2 cleavage: Glu487 in Fet3p (Asp452 in Cg L), located in the vicinity of the TNC, acts as a proton donor, determining the pH–activity profile (Augustine *et al.*, 2007; Chen *et al.*, 2010), while Asp94 in Fet3p (Asp76 in Cg L) deprotonates the T2 Cu water ligand, driving electron transfer from the T1 Cu to the TNC (Fig. 1).

X-ray-determined three-dimensional structures of BMCOs from different sources have provided valuable information about substrate binding (Kallio *et al.*, 2009; Matera *et al.*, 2008), intermediate structures (Bento *et al.*, 2005), proton donors (Taylor *et al.*, 2005) and structural determinants of the reduction potential of the T1 Cu (Hall *et al.*, 1999; Piontek *et al.*, 2002; Ravelli & Garman, 2006). However, the effects of ionizing radiation on metal sites have frequently been ignored. As a consequence of the interaction of X-rays, particularly with solvent, radiolysis of the latter occurs, releasing radicals that react both locally and at distances of a few micrometres (O'Neill *et al.*, 2002), causing damage to the protein moiety (Garman, 2010). Specific damage is observed at the electron-density level in the following order: metal reduction and radiolysis, disulfide-bond breakage, decarboxylation of aspartic and glutamic acids, OH^- scission from tyrosines and breakage of the C—S bond in methionines (Burmeister, 2000; Ravelli & McSweeney, 2000; Weik *et al.*, 2000; Oliéric *et al.*, 2007; Macedo *et al.*, 2009). Metal reduction and radiolysis are of particular relevance for redox-active metal sites, where the oxidation state determines their structure (Messerschmidt *et al.*, 1993), limiting the biological interpretation derived from the structural information. In the specific case of laccases, the presence of different intermediates of O_2 reduction has been reported in structures from different sources (Piontek *et al.*, 2002; Bento *et al.*, 2005; Polyakov *et al.*, 2009), of different monomers in the asymmetric unit (Ferraroni *et al.*, 2007) and even of crystals subjected to various absorbed doses (Hakulinen *et al.*, 2006). Notably, Hakulinen *et al.* (2006) analysed the X-ray-induced reduction process in crystals of *Melanocarpus albomyces* laccase using a UV–Vis microspectrophotometer coupled to an in-house diffractometer. They found that the intensity of the 610 nm peak diminished gradually after 6, 18, 24 and 48 h of exposure to X-rays and showed that the blue colour characteristic of T1 Cu disappeared from the regions irradiated with X-rays. The authors also found that in some crystals the peaks at 320 and 420 nm remained unchanged after 48 h of X-ray radiation exposure, even after T1 Cu reduction, while in others these peaks diminished during 24 h of exposure. Additionally, the authors found that crystals subjected to high absorbed doses presented a hydroxyl moiety in the TNC instead of the O_2 observed at lower doses. Together, these observations exposed the susceptibility of copper centres to X-ray-induced reduction and the need to quantitate the absorbed dose during diffraction experiments.

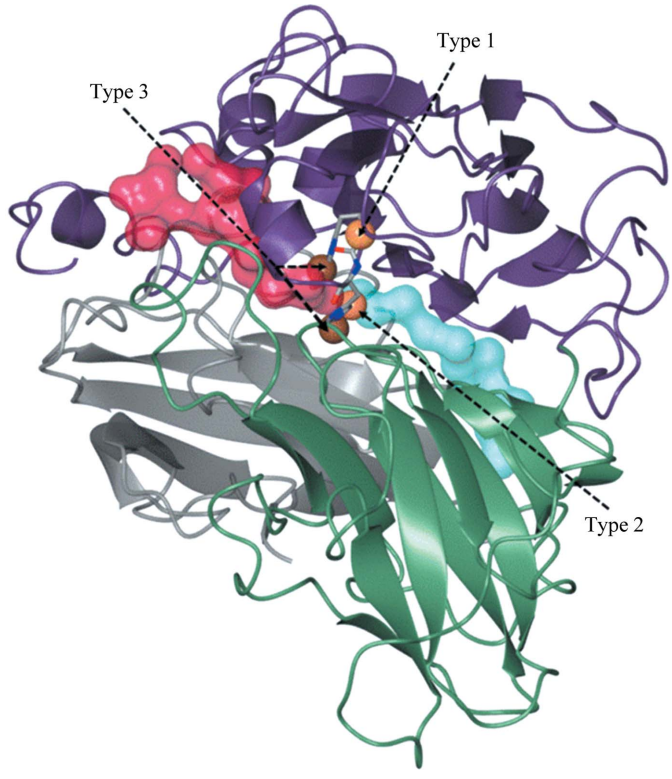

Figure 1
The Cg L fold, showing the copper-centre distribution for the three cupredoxin domains (domain 1, grey; domain 2, green; domain 3, purple) and the dioxygen-entrance (red) and water-exit (blue) channels.

Here, we describe the X-ray-determined three-dimensional structure of the laccase from the basidiomycete *Coriolopsis gallica* (Cg L), a high catalytic potential BMCO previously studied for its ability to decolorize textiles and to oxidize polycyclic aromatic hydrocarbons (PAHs; Pickard *et al.*, 1999). Taking advantage of photoreduction processes occurring principally at copper ions during X-ray diffraction, as confirmed by X-ray absorption spectroscopy (XAS), we were able to obtain different structures showing changes in T1 Cu coordination distances and TNC geometrical conformation by manipulating the pH and the X-ray radiation dose absorbed by the Cg L crystals. A correlation between copper-centre conformation and absorbed dose was observed, highlighting the importance of considering these issues during structure determination and interpretation of the X-ray structures of metalloproteins.

2. Methods

All chemical supplies were of analytical grade and purchased from Sigma–Aldrich, unless otherwise stated.

2.1. Protein purification

Cg L isolated from the basidiomycete *C. gallica* was purchased from IBMol (Mexico). The gene sequence translates to 517 residues, of which the first 21 are part of a signal peptide that is removed after the protein is exported to the extracellular space. The final product is a 496-residue protein with a molecular weight of 52.7 kDa and an estimated extinction coefficient of 60.5 mM^{-1} cm^{-1} at 280 nm as calculated using the *Protein Calculator* v.3.3 software (http://www.scripps.edu/~cdputnam/protcalc.html). The sample was approximately 70% pure based on SDS–PAGE analysis. The protein was purchased as a light-blue solution containing 0.1 *M* potassium phosphate pH 6 and 20%(*v*/*v*) glycerol. This solution was first dialyzed against 50 m*M* MES pH 5.5 using a 14 kDa molecular-weight cutoff membrane in order to eliminate glycerol and other low-molecular-weight impurities. A second dialysis and concentration step was performed in Amicon Ultra tubes (30 kDa molecular-weight cutoff; Millipore). After centrifugation, 2 ml of a 2 mg ml^{-1} protein solution was applied onto a HiLoad 26/60 Superdex 200 gel-filtration column (GE Life Sciences) previously equilibrated with 50 m*M* MES, 50 m*M* NaCl pH 5.5. A predominant clear well defined absorbance peak corresponding to the molecular weight of Cg L was observed at 280 nm on the chromatogram. Purity higher than 95% and a molecular weight of 57 kDa was confirmed by SDS–PAGE and IEF gels (data not shown; the difference from the molecular weight calculated from the sequence arises from the glycosylation of at least two Asn residues). The calculated isoelectric point (pI) from the IEF gel was 3.5. Finally, a 2 h incubation in 0.5 m*M* $CuSO_4$ was performed in order to ensure full occupancy of the copper sites, which was followed by dialysis against 20 m*M* MES pH 5.5 to remove NaCl and unbound copper. Protein concentration was determined by Bradford assays (Bio-Rad; Bradford, 1976).

2.2. Copper content

Copper quantification was performed by the 2,2′-biquinoline method, as described previously (Felsenfeld, 1960). A 5 mg ml^{-1} 2,2′-biquinoline solution in 50%(*v*/*v*) acetic acid was prepared and standardized against five submillimolar solutions of $CuSO_4$ incubated in 2 m*M* ascorbic acid, from which an $\varepsilon_{546\,nm}$ = 6.8 mM^{-1} cm^{-1} was determined, consistent with previous reports (Hanna *et al.*, 1988). Protein solutions (50 µl at ∼20 mg ml^{-1}) were incubated in 2 m*M* ascorbic acid for 20 min to reduce cupric ions to Cu^{I} and were then mixed with 50 µl of the 2,2′-biquinoline solution. Solutions were kept anaerobic by bubbling gaseous N_2 through them.

Copper stoichiometries were also quantified by MicroPIXE (Garman, 1999; Garman & Grime, 2005). Purified protein was extensively dialyzed against 50 m*M* Tris–HCl pH 7.2, 5%(*v*/*v*) PEG 1000, and 5%(*v*/*v*) PEG 8000 to eliminate sulfur from the MES solution and to emulate the crystallization conditions. Two 0.2 µl drops of a 10 mg ml^{-1} Cg L solution were dried onto a 4 µm thick polypropylene film mounted over a hole in an aluminium target holder. In order to identify the protein in the dried drop, a coarse 1 mm^2 scan over the protein drop was collected using a 2.5 MeV proton microbeam (3 µm diameter). The induced characteristic X-ray emission spectrum from the sample under vacuum was detected in a solid-state lithium-drifted silicon detector. Upon scanning in the *x* and *y* dimensions, spatial maps were obtained of all elements heavier than Ne that were present in the sample. Quantitative information was obtained by averaging two spectra collected at selected points on the sample. Spectral analysis was carried out using *GUPIX* (Johansson *et al.*, 1995) to determine the concentration of copper in the sample relative to the sulfur signal from the five cysteine and four methionine residues contained in Cg L. All data were collected at the Ion Beam Centre, University of Surrey, England on a beamline arranged as described previously (Grime *et al.*, 1991).

2.3. Activity measurements and UV–visible spectra

Substrate oxidation was followed spectrophotometrically using both phenolic (2,6-dimethoxyphenol; DMP; $\varepsilon_{468\,nm}$ = 27.5 mM^{-1} cm^{-1}) and nonphenolic [2,2′-azino-bis(3-ethylbenzothiazoline-6-sulfonic acid) diammonium salt; ABTS; $\varepsilon_{436\,nm}$ = 29.3 mM^{-1} cm^{-1}] substrates. UV–visible spectra were recorded with an Evolution 1000 spectrophotometer (Thermo Scientific) using 1 cm path-length quartz cells. Spectra were recorded over the 260–900 nm interval. Several measurements were taken against a blank with a protein-free buffer and using different buffer systems at three pH values: 50 m*M* MES pH 5.5 and 4.0, 50 m*M* Tris–HCl pH 7.0 and 50 m*M* citrate pH 4.0, 5.5 and 7.0. Copper oxidation was tested by adding hydrogen peroxide (H_2O_2) to the protein solution.

2.4. Electron paramagnetic resonance

Electron paramagnetic resonance (EPR) spectra were recorded in the X and W bands using 20 mg ml^{-1} Cg L solutions in 50 m*M* MES pH 4.0 and 5.5 and in 50 m*M* Tris–HCl pH 7.0. Continuous-wave (CW) X-band spectra were recorded using a Bruker EMX spectrometer with a helium cryostat (Oxford Cryosystems) at 30 or 40 K under nonsaturating conditions. W-band electron spin-echo-detected field-sweep spectra were measured using a Bruker E680 spectrometer at 12.5 K. The W-band spectra were used in order to aid simulations of X-band CW spectra, which were carried out using scripts written around *EasySpin* (Stoll & Schweiger, 2006). Each distinct copper signal was simulated with an anisotropic (although mostly axial) *g*-tensor, a *g*-strain (constant for all samples), an H-strain and an axial hyperfine tensor (with the perpendicular component always set at 30 MHz). The relative ratios of the copper signals were determined from the areas of the absorption-type (zeroth harmonic) spectrum.

2.5. Electrochemistry

The catalytic potential ($E_{\rm cat}$) of Cg L and its pH dependence were determined by protein-film electrochemistry experiments carried out in a sealed, jacketed, temperature-controlled all-glass cell using a modified pyrolytic graphite edge (PGE) rotating-disk working electrode (projected area 3 mm^2) in conjunction with a Princeton Applied Research 636 electrode rotator, a platinum-wire counter electrode and an Ag|AgCl|3 *M* NaCl reference electrode. The reference electrode was housed in a side arm filled with 0.1 *M* Na_2SO_4 and connected to the cell by a Luggin capillary. The reference potential was corrected to the standard hydrogen electrode (SHE) using $E_{\rm SHE} = E_{\rm Ag|AgCl} + 0.206$ V at 298 K. The voltammetry was controlled by an Ivium CompactStat. The electrode surface was modified with anthracene moieties as described previously (Blanford *et al.*, 2007). The potential of the rotating electrode was cycled once between 0.5 and −0.3 V (*versus* SCE) in an acidic 0.19 m*M* solution of anthracene-2-diazonium formed from its corresponding amine and held at 273 K. A protein 'film' was formed upon the addition of 2 µl of an 18 mg ml^{-1} Cg L solution to the freshly modified electrode. Electrocatalytic measurements were carried out in buffer equilibrated with 100% O_2 at 298 K by flowing the gas through the enclosed headspace over the rapidly agitated solution. The electrode was rotated at 4000 rev min^{-1}, so the effect of O_2 transport on the electrocatalytic response of the enzyme was negligible. The catalytic potential $E_{\rm cat}$ was calculated from the maximum of the first derivative of the third scan from the cyclic voltammetry measurements using the *SOAS* software (Fourmond *et al.*, 2009).

2.6. Crystallization

Prior to crystallization trials, the protein solution was dialyzed against 10 m*M* MES pH 5.5 to remove NaCl and copper ions from solution. Crystal Screen and Crystal Screen 2 from Hampton Research (Laguna Niguel, California, USA) were chosen as starting points in the search for crystallization conditions. The protein was concentrated to 15 mg ml^{-1} and 1 + 1 µl drops were set up using the hanging-drop method. Microcrystals were obtained in condition No. 7 of Crystal Screen 2 (Hampton Research) consisting of 10%(*w*/*v*) PEG 1000, and 10%(*w*/*v*) PEG 8000. Upon optimization, 0.20 × 0.25 × 0.20 mm crystals were observed at 277 K after 48 h in the following conditions: (i) 100 m*M* MES pH 4.0, 5%(*w*/*v*) PEG 1000, 5%(*w*/*v*) PEG 8000 and (ii) 100 m*M* Tris–HCl pH 7.0, 10%(*w*/*v*) PEG 1000, 10%(*w*/*v*) PEG 8000. Attempts to grow crystals in acetate or citrate buffer at acidic pH were unsuccessful. Crystals at pH 5.5 were obtained by gradual replacement of the 50 m*M* Tris–HCl pH 7.0 mother liquor, in which the crystals were originally grown, by 50 m*M* MES pH 5.5. All pH values were verified with pH-paper test strips (pHydrion; pH ranges 1–12 and 0–6) and with a pH meter (Oakton Benchtop Meter 510) after scaling solutions to a 10 ml volume. Prior to data collection, the crystals were transferred into a cryoprotectant solution consisting of 25%(*w*/*v*) PEG 1000, 15%(*w*/*v*) PEG 400, 5%(*w*/*v*) PEG 8000 and the desired buffer solution at 100 m*M*. The crystals were mounted in rayon cryoloops and flash-cooled in a nitrogen stream at 100 K. In order to increase copper-site occupancies, crystals grown at pH 4.0 and 7.0 were soaked in the cryoprotectant solution described above but with the substitution of water by 10 m*M* $CuSO_4$ or $CuCl_2$ (Bento *et al.*, 2005) for 10 min. At soaking times longer than 10 min the crystals showed visible cracks and lost diffracting power regardless of the copper salt used.

The enzymatic activity of the crystals was tested by soaking them in a solution in which 2 m*M* DMP replaced water in the precipitant solution. Colour changes from blue to orange characteristic of the DMP oxidized product 3,3-5,5-tetramethoxy-4,4′-biphenylquinone were observed using an optical microscope.

2.7. X-ray data collection

In-house data collection was performed using a Rigaku RU-200H X-ray generator equipped with Yale mirrors operated at 90 kV and 50 mA and producing λ = 1.5418 Å X-rays, with an Oxford Cryosystems 600-series cryostream and an R-AXIS IV detector (Rigaku). Alternatively, data collection took place on NSLS beamline X6A at two X-ray wavelengths, 0.9795 Å (12 659 eV) and 1.3778 Å (8999 eV), using an Oxford Cryosystems 700 series cryostream and an ADSC Q270 CCD detector (ADSC, Poway, California, USA). X-ray absorption spectra were collected in fluorescence mode on beamline X6A at the NSLS in the energy interval 8950–9130 eV using an Si(111) channel-cut monochromator (band pass: 1.9 × 10^{-1} eV) and a custom-made fluorescence detector vertically positioned at an angle of 90° relative to the beam axis. Spectra were recorded before and after a complete data set had been collected in order to characterize the oxidation state at the lowest achievable dose and after the collection of a complete data set; the estimated absorbed dose per scan was 0.2 MGy. Fluorescence spectra were subjected to background subtraction and normalized using the *Athena* software package (Ravel

Table 1
EPR parameters obtained from protein solutions at different pH values.

Values in parentheses are for an alternative T2 Cu population (T2′ Cu) observed at acidic pH.

	Parameter	pH 4.0	pH 5.5	pH 7.0
CuT1	g_x	2.045	2.05	2.06
	g_y	2.05	2.035	2.05
	g_z	2.192	2.188	2.192
	A (cm^{-1})	10×10^{-4}	10×10^{-4}	10×10^{-4}
	$A_{\|\|}$ (cm^{-1})	93×10^{-4}	90×10^{-4}	93×10^{-4}
CuT2 (CuT2′)	g_x	2.05 (2.08)	2.05 (2.075)	2.05
	g_y	2.03 (2.08)	2.03 (2.075)	2.03
	g_z	2.26 (2.365)	2.26 (2.260)	2.263
	A (cm^{-1})	10×10^{-4}	10×10^{-4}	10×10^{-4}
	$A_{\|\|}$ (cm^{-1})	177×10^{-4} (153×10^{-4})	177×10^{-4} (153×10^{-4})	170×10^{-4}

& Newville, 2005). Absorbed dose calculations were carried out using *RADDOSE* v.2 (Murray *et al.*, 2004; Paithankar *et al.*, 2009). In order to calculate the absorbed dose, values of the beam parameters (including the energy, profile, size/area and flux) and crystal properties (unit cell, space group, number of molecules per asymmetric unit, composition, size and thickness) were used. An estimate of the beam flux in photons s^{-1} was obtained by using a silicon pin diode to calibrate the beam intensity, as described previously (Owen *et al.*, 2009).

UV–Vis absorption spectra were collected from Cg L solutions using the online microspectrophotometer on beamline ID14-4 at the ESRF (McGeehan *et al.*, 2009). Spectra were collected from a cryocooled 20 mg ml^{-1} Cg L solution containing 25% PEG 1000, 15% PEG 400 and 5% PEG 8000 in 100 m*M* MES buffer pH 5.5 held in a rayon cryoloop at 100 K. An initial loop orientation was determined to maximize the 280 nm absorption peak. Spectra were recorded every 307 ms for 4 min 20 s in the range 200–1100 nm using the *OOIBase*32 software (Ocean Optics). After 20 s of data recording, the sample was subjected to 30 1 s X-ray irradiations with around 3 s (corresponding to the detector readout time) between each exposure to give a total of 120 s, followed by a 120 s spectra-collection period with the beam off. The incident X-ray beam of dimensions 50 × 100 µm and wavelength 0.9395 Å (13 198 eV) was used at 100% transmission.

2.8. Data processing and model refinement

Indexing and integration of diffraction data were performed using *MOSFLM* (Leslie, 2006). Integrated reflections were sorted, scaled and truncated with *SORTMTZ*, *SCALA* and *TRUNCATE* (Evans, 2006), respectively, from the *CCP*4 suite (Winn *et al.*, 2011). Molecular replacement was carried out in *MOLREP* (Vagin & Teplyakov, 2010) with a homology-based model constructed using *SWISS-MODEL* (Bordoli *et al.*, 2009). Briefly, the Cg L sequence (AAF70119.2) deposited in GenBank (Benson *et al.*, 2011) was aligned with sequences extracted from PDB-deposited structures of the fungal BMCOs from *Trametes versicolor* (PDB entry 1kya; Bertrand *et al.*, 2002), *Coprinus cinereus* (PDB entry 1hfu; Ducros *et al.*, 2001) and *Rigidoporus lignosus* (PDB entry 1v10; Garavaglia *et al.*, 2004) using *ClustalW* (Larkin *et al.*, 2007). The resulting model was subjected to rigid-body refinement followed by restrained refinement in *REFMAC*5 (Murshudov *et al.*, 2011). The sequence was confirmed by evaluating the fit of the model to the $F_o - F_c$ electron-density maps from the pH 5.5 data set collected in-house to a resolution of 1.65 Å. *Coot* (Emsley *et al.*, 2010) was used for manual model building and addition of copper ions, glycans and water molecules. Glycosylation sites had previously been monitored using *NetNGlyc* (Zhu *et al.*, 1998). During refinement, atomic displacement parameters (ADPs) for all coppers were initially calculated with a fixed occupancy. Once convergence was reached, the occupancies of such atoms were calculated iteratively in *PHENIX* v.1.5 (Adams *et al.*, 2010). Refinement cycles ended when R_{work} and R_{free} values lower than 0.20 and 0.25, respectively, were obtained. Coordinate errors were obtained from the estimated standard error (e.s.u.) in atomic positions calculated using

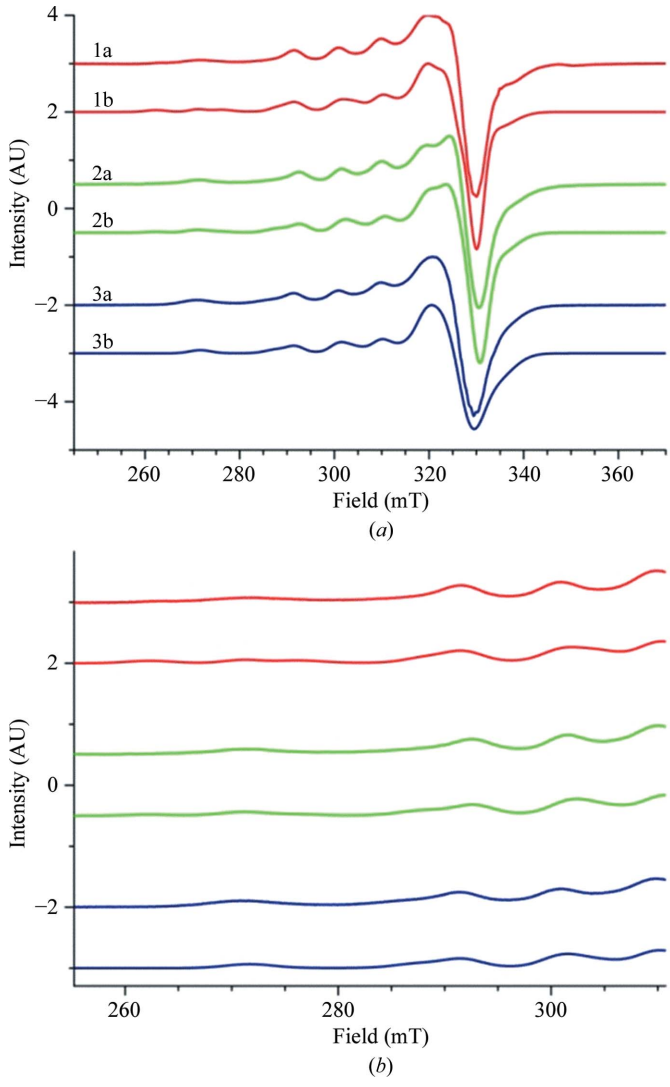

Figure 2
(*a*) CW EPR spectra collected from Cg L solutions at different pH values (red, green and blue correspond to pH 4.0, 5.5 and 7.0, respectively, while 1a and 1b refer to experimental data and simulation, respectively). (*b*) Magnification of the T2 Cu region showing the pH-induced changes caused at this metal centre.

REFMAC from R_{work} and R_{free}. Considering that e.s.u. values represent an average uncertainty for each structure, copper–ligand bond distances are expected to have higher precision because of their lower displacement parameters relative to the entire atomic ensemble (Vaguine *et al.*, 1999). Model validation was performed using *PROCHECK* (Laskowski *et al.*, 1993). $F_o - F_o$ difference maps were calculated using *SORTMTZ*, *SCALEIT* and *FFT*. All of the above programs except for *ClustalW*, *SWISS-MODEL* and *PHENIX* are contained in the *CCP*4 suite (Winn *et al.*, 2011).

Composite data sets for four different absorbed doses were obtained using the method described previously (Berglund *et al.*, 2002). Briefly, complete diffraction patterns were collected from four Cg L crystals at different known starting φ angles. Each data set consisted of 240 images of $\Delta\varphi = 0.5^\circ$ each (120° total rotation). Four groups of 80 images per data set were formed, with each group corresponding to a different absorbed dose. Images corresponding to the same absorbed dose were merged using *SORTMTZ* in order to form composite data sets corresponding to increasing doses. The data sets were then processed as described above.

3. Results

3.1. Copper quantitation

The two methods used to determine the copper content in purified Cg L confirmed that the protein contained four Cu atoms. The 2,2′-biquinoline method resulted in a ratio of 3.8 ± 0.4 Cu atoms per protein molecule, with no significant differences depending on the pH of the buffer solution utilized (data not shown). MicroPIXE data were collected from two independent preparations. A metal content of 4.2 ± 0.2 Cu atoms per molecule of Cg L was determined for both samples, supporting the observation that the pure enzyme contained the full complement of coppers (T1 Cu, T2 Cu and T3 Cu) even at acidic pH and in the presence of PEG 1000 and PEG 8000 employed during crystallization, although low occupancies were observed in the crystallographic structure (see §3.3).

3.2. UV–visible and EPR spectroscopy

UV–visible spectroscopic characterization of Cg L in solution resulted in normal extinction coefficients for the T3 Cu (near-UV-absorbing) and the single 'blue' T1 Cu coppers, respectively: $\varepsilon_{T3} = 10.1\ mM^{-1}\ cm^{-1}$ and $\varepsilon_{T1} = 4.2\ mM^{-1}\ cm^{-1}$ at pH 5.5 (Table 1). Cg L incubated in the presence of peroxide or alternatively in 1 m*M* $CuSO_4$ solution [either as Cu^{II} or kept in the reduced form Cu^{I}; data not shown] did not increase the absorbance at 330 nm (T3 Cu) or at 608 nm (T1 Cu), ruling out the possibility of a partially reduced or occupied population. No significant differences were observed when comparing ε_{T1} and ε_{T3} at pH values of 4.0, 5.5 and 7.0 (not shown).

The X-band EPR spectra for Cg L at pH 4.0, 5.5 and 7.0 are shown in Fig. 2(*b*) together with corresponding simulations. The W-band spectra are not shown, but their salient features were used to guide simulation of the X-band data. The parameters for the simulations are shown in Table 1. The pH 7.0 result was simulated well by a 1:1 ratio of two types of copper signals: the first corresponding to T1 Cu with $A_{\|} = 93 \times 10^{-4}\ cm^{-1}$ and the second corresponding to T2 Cu with $A_{\|} = 170 \times 10^{-4}\ cm^{-1}$. In order to simulate the pH 5.5 spectra, an additional copper signal was required, as well as some small variation in the copper signal parameters from the pH 7.0 simulation. The signal had $A_{\|} = 153 \times 10^{-4}\ cm^{-1}$ and is therefore designated T2′ Cu. This copper signal was modelled as 1/8 of the total signal, with the original T2 Cu spectrum accounting for 3/8 and the T1 Cu for the remaining 1/2. In a similar manner, the pH 4.0 spectrum could be simulated well by assuming a 2:1:1 ratio of T1 Cu:T2 Cu:T2′ Cu, where the two T2 and T2′ Cu signals are different from one another but have similar parameters to those used to simulate the pH 5.5 spectra, while the T1 Cu has similar parameters to those used at both pH 5.5 and 7.0. The EPR data show that there is a

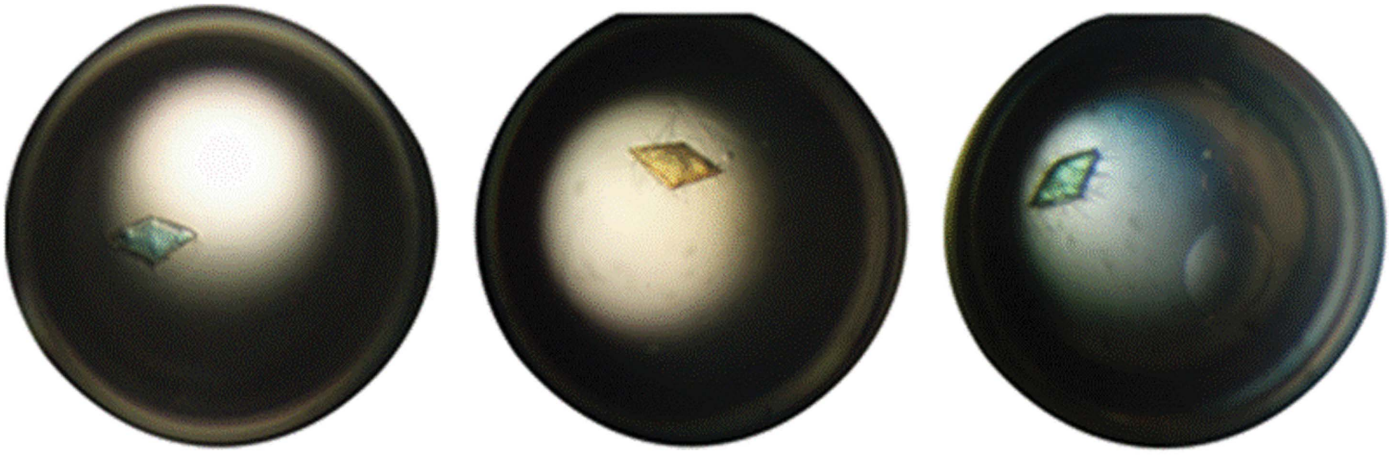

Figure 3
Active crystals of Cg L grown in 5% PEG 1000, 5% PEG 8000, and 100 m*M* MES pH 4.0: (*a*) 2 min after soaking in 2 m*M* DMP, (*b*) 30 min after soaking, (*c*) 60 min after soaking.

Table 2
Data-collection statistics.

Values in parentheses are for the last shell.

Data set	pH 4.5	pH 5.5	pH 7.0	0.98 Å	1.38 Å
Space group	$P2_12_12_1$	$P2_12_12_1$	$P2_12_12_1$	$P2_12_12_1$	$P2_12_12_1$
Unit-cell parameters (Å)					
a	56.06	56.38	56.47	56.03	55.01
b	85.45	86.13	86.21	85.55	85.23
c	151.75	152.64	152.24	151.56	151.51
Mosaicity (°)	0.72	0.47	0.71	0.79	0.43
Residues per monomer	496	496	496	496	496
Monomers per asymmetric unit	1	1	1	1	1
Matthews coefficient ($Å^3$ Da^{-1})	3.26	3.44	3.32	3.23	3.21
Solvent content (%)	62.26	64.20	62.98	61.90	61.76
X-ray source	Rigaku RU-200H			NSLS X6A	NSLS X6A
Detector	R-AXIS IV image plate			Quantum 270 CCD	Quantum 270 CCD
Wavelength (Å)	1.5418			0.9795	1.3778
Resolution range (Å)	34.7–2.30 (2.40–2.30)	24.45–1.65 (1.74–1.65)	34.7–2.30 (2.40–2.30)	34.7–1.90 (2.00–1.90)	34.7–1.80 (1.90–1.80)
Unique reflections	32606	87114	32281	52446	64137
Multiplicity	3.6 (3.6)	3.2 (2.5)	3.3 (2.7)	4.4 (4.4)	2.5 (2.5)
Completeness (%)	98.8 (98.8)	93.7 (79.5)	95.8 (85.9)	91.2 (95.5)	95.2 (95.0)
$\langle I/\sigma(I)\rangle$	5.4 (1.9)	9.8 (2.3)	5.8 (2.6)	4.5 (2.9)	11.2 (4.2)
R_{merge} (%)	11.0 (41.0)	5.1 (27.0)	9.8 (29.3)	11.5 (23.4)	4.4 (17.6)
Wilson plot *B* value ($Å^2$)	36.40	17.68	35.80	13.14	16.88

Table 3
Refinement statistics.

Data set	pH 4.5	pH 5.5	pH 7.0	0.98 Å	1.38 Å
R_{work}/R_{free} (%)	19.72/22.67	15.36/18.72	18.86/22.46	18.56/22.38	15.76/19.48
Contents of asymmetric unit					
Protein atoms	496	496	496	496	496
Copper ions	3	4	4	3	2
Water molecules	312	606	312	415	652
R.m.s.d. from ideal					
Bond lengths (Å)	0.010	0.012	0.010	0.025	0.007
Bond angles (°)	1.34	1.50	1.279	2.12	1.367
Mean overall *B* value ($Å^2$)					
Protein	25.80	13.98	24.82	23.22	16.56
Solvent	30.18	26.72	29.59	31.06	28.82
Ramachandran plot, residues in					
Most favoured regions	463 (93.91%)	467 (94.72%)	464 (94.12%)	464 (94.12%)	465 (94.32%)
Additionally allowed regions	28 (5.68%)	24 (4.86%)	27 (5.48%)	27 (5.48%)	26 (5.07%)
Outliers	2 (0.41%)	2 (0.41%)	2 (0.41%)	2 (0.41%)	2 (0.41%)
Estimated absorbed dose (MGy)	0.2	0.6	0.3	16	5.9
PDB code	4a2d	4a2e	4a2h	4a2f	4a2g
No. of images collected ($\Delta\varphi = 0.5°$)	180	198	200	250	200

constant ratio of T1 Cu to T2 Cu and, while there are some minor conformational changes around the T1 Cu site associated with pH, the main change is an alternative T2 Cu configuration, which appears to increase in concentration with decreasing pH values.

3.3. Crystallographic structures

To prove that Cg L maintained its activity in crystalline conditions, crystals grown at pH 4.0 and 7.0 were soaked in a solution identical to the mother-liquor solution but containing 2 m*M* DMP. A colour change from blue to orange in Cg L crystals grown at pH 4.0 was observed 30 s after substrate addition (Figs. 3*a* and 3*b*), indicating the appearance of oxidized DMP product. After 30 min, the substrate was consumed and the Cg L crystal recovered its characteristic blue colour (Fig. 3*c*). No visible colour changes were observed in crystals grown at pH 7.0, demonstrating that pH inhibition occurs even in protein crystals.

3.3.1. Cg L structure. All structures determined in this work belonged to space group $P2_12_12_1$, with small variations in unit-cell parameters ($a = 56.13 \pm 0.38$, $b = 85.62 \pm 0.70$, $c = 151.83 \pm 0.85$ Å; Table 3) and a solvent content of 62.6 ± 1.6%. Electron density corresponding to N-linked glycosylation was only observed at two (Asn54 and Asn433) of the five potential N-glycosylation sites (Asn51, Asn54, Asn207, Asn335 and Asn433). At least two *N*-acetylglucosamine molecules were clearly distinguishable in $F_o - F_c$ maps at a level of 3.5σ and were included in the final model. Data-reduction and refinement details are given in Tables 2 and 3, respectively. Variations in occupancies for all copper ions were observed as a consequence of pH and absorbed dose differences (Table 4; discussed below).

Table 4
Copper-to-ligand coordination distances and occupancies for the three copper sites in Cg L determined at different pH values.

	T1 Cu		T2 Cu	T3 Cu		
pH	Distance (Å)	Occupancy	Occupancy	Cu_A–Cu_B distance (Å)	Occupancy	Coordinate error (maximum-likelihood-based) (Å)
4.0	His415 N–Cu, 2.0 His476 N–Cu, 2.6 Cys471 S^{γ}–Cu, 2.2	0.3	—	4.5	A = 0.8, B = 0.7	0.14
5.5	His415 N–Cu, 2.0 His476 N–Cu, 2.1 Cys471 S^{γ}–Cu, 2.2	0.7	0.46	5.0	A = 0.8, B = 0.8	0.05
7.0	His415 N–Cu, 2.0 His476 N–Cu, 2.1 Cys471 S^{γ}–Cu, 2.1	0.60	0.31	4.8	A = 0.8, B = 0.6	0.12

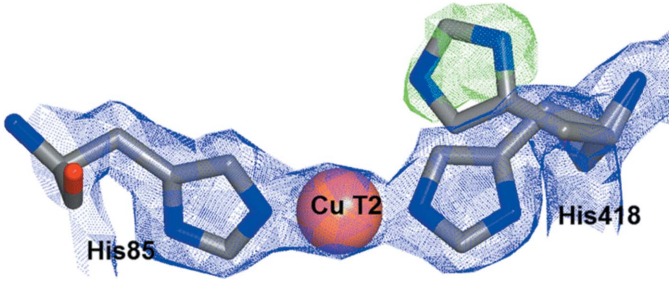

Figure 4
Alternative conformation of the T2 Cu-coordinating His418 fitted into positive density in the $F_o - F_c$ map (green). $2F_o - F_c = 1.5\sigma$ (blue) and $F_o - F_c = 3.5\sigma$ (green) electron densities are displayed and correspond to the crystal at pH 5.5.

The overall architecture of Cg L is identical to those of previously reported fungal BMCOs; calculated r.m.s.d. values of 0.32, 0.52 and 0.81 Å were obtained after superimposing 490 C^{α} atoms with *Trametes trogi* (PDB entry 2hrh; A. Gullotto, I. Matera, S. Tilli, M. Ferraroni, F. Briganti & A. Scozzafava, unpublished work), *T. versicolor* (PDB entry 1kya; Bertrand *et al.*, 2002) and *C. cinereus* (PDB entry 1hfu; Ducros *et al.*, 2001) laccase structures, respectively. The four reactive copper ions are distributed among two of the three cupredoxin domains; while T1 Cu and all residues involved in its first and second coordination spheres are located in domain 3, the TNC, formed by T2 Cu and T3 Cu, is located in the interface between domains 1 and 3. TNC-coordinating residues are equally distributed in both domains, while T1 Cu is coordinated by His415, His476 and Cys471, all of which are located in domain 3 (Ducros *et al.*, 1998). Flanking the metal site, Ile473 and Phe481, which are located 3.9 and 3.7 Å from T1 Cu, respectively, are part of a hydrophobic region in the vicinity of T1 Cu.

3.3.2. pH effects. The most significant differences between the structures derived from in-house diffraction data collected from crystals at different pH values were observed at the copper centres. The T1 Cu coordination distances at pH 5.5 and 7.0 correspond to the average canonical distances for this type of metal centre observed in crystallographic structures deposited in the PDB; for Cg L, these are His415 N^{δ}–Cu = 2.0 Å, His476 N^{δ}–Cu = 2.1 Å and Cys471 S^{γ}–Cu = 2.2 Å (Table 4). Electron density for the T1 Cu and all three copper ions of the TNC was observed in OMIT maps at a σ level higher than 8.4 for the pH 5.5 and 7.0 structures. After including copper ions in the model, an additional positive electron-density peak between T3 Cu_A and T3 Cu_B was observed in $F_o - F_c$ maps at a σ level of 3.5 in both the pH 5.5 and 7.0 structures. A water molecule corresponding to an intermediate of O_2 reduction was modelled at unequal distances from the two copper ions forming the T3 Cu. In contrast to the ascomycete *M. albomyces* laccase (PDB entries 2q9o and 2ih8; Hakulinen *et al.*, 2006, 2008), in which the TNC geometry corresponds to an isosceles triangle, in Cg L the geometry corresponds to a scalene triangle in which T3 Cu_A and T3 Cu_B are ∼5 Å (4.9 ± 0.13 Å) apart while the T3 Cu_A–T2 Cu and T3 Cu_B–T2 Cu distances are 4.4 and 4.0 Å, respectively. Structures with this geometry have previously been described in other basidiomycete laccases (Piontek *et al.*, 2002) as characteristic of the oxidized state.

Furthermore, additional positive density close to the side chain of His418 was observed during inspection of an $F_o - F_c$ electron-density map at a σ level of 3.5 for the pH 5.5 structure (Fig. 4). The positive peak disappeared upon the addition of an alternative conformation of His418 with a refined occupancy of 0.3. This alternative conformation places His418 N^{ε} at a coordination distance of 2.6 Å from the T3 Cu_A copper site, causing the T3 Cu_A site to become pentacoordinated.

At pH 4.0, positive peaks in the $F_o - F_c$ maps for T1 Cu and T3 Cu were observed at 4.9σ and 11.0σ, respectively. However, the lower peak at the T1 Cu in the pH 4.0 structure compared with both T3 Cu and T1 Cu in the electron-density maps derived from the pH 5.5 and 7.0 crystals indicates a significantly lower occupancy at pH 4.0. While the refined occupancies at pH 5.5 and 7.0 are higher than 0.6, at pH 4.0 the site presents a refined occupancy of only 0.3 (Table 4). In addition to the decrease in occupancy, changes in the ligand-to-metal coordination distances were also observed. A significant increase from 2.1 to 2.6 Å was found in the His476 N^{δ}–T1 Cu coordination bond distance (Figs. 5*a* and 5*b*). Additionally, a depleted T2 Cu was found in the pH 4.0 structure: no electron density was observed in the site corresponding to T2 Cu in $F_o - F_c$ maps at 3.0σ. Partial occupancy of this site has been commonly observed in crystal structures of several BMCOs deposited in the PDB (entries 2h5u, 3gdc, 2zwn, 2bhf and 1uvw; Lyashenko *et al.*, 2006; I. S. MacPherson, W. C. Lee, T. I. Liang & M. E. P. Murphy, unpublished work; Komori *et al.*, 2009; Bento *et al.*, 2005; Enguita *et al.*, 2004), but complete depletion has previously only been reported in *C. cinereus* laccase structures (PDB entries 1a65 and 1hfu; Ducros *et al.*, 1998, 2001). Moreover, significant differences were also observed in the T3 Cu_A–T3 Cu_B distance after superposing the

Cg L pH 4.0 and pH 5.5/7.0 structures. There is a contraction of 0.4 Å in the T3 Cu_A–T3 Cu_B distance from the 4.9 ± 0.13 Å observed at pH 5.5 and 7.0 to 4.5 Å at pH 4.0 (Figs. 5*c* and 5*d*; Table 4). The absence of electron density between the T3 Cu ions suggests that this structure corresponds to a more reduced state (see §4).

3.4. Effects of higher absorbed radiation doses on Cg L crystals

To assess the effects of higher absorbed radiation doses and different X-ray energies, crystals grown at pH 4.0 and 7.0 were exposed on NSLS beamline X6A at incident wavelengths of 0.9795 and 1.3778 Å (12 659 and 8999 eV, respectively). It is worth noting that the absorbed dose per data set at this X-ray source is about eight times higher than the dose absorbed by crystals when exposed on our in-house X-ray source (Table 3). Structures from all crystals grown at pH 4.0 showed depletion at both T1 Cu and T2 Cu sites independent of the dose or the wavelength employed, in contrast to the structure determined using our in-house source at an absorbed dose of 0.62 MGy, in which the T1 Cu was present with an occupancy of 0.3. Additionally, the T3 Cu_B sites of crystals exposed at the synchrotron also showed an occupancy that was lower by 0.3 on average than those exposed to our in-house source (0.5 *versus* 0.8, respectively). However, structures from the crystals grown at pH 7.0 derived from synchrotron data showed depletion of T2 Cu but had occupancies lower than 0.2 at T1 Cu (at incident X-ray wavelengths of both 0.98 and 1.38 Å; Table 4).

Anomalous electron-density maps calculated from data sets for Cg L crystals collected at the experimentally calculated Cu *K* edge (1.3778 Å, 8999 eV; NSLS beamline X6A) as determined following fluorescence scans showed anomalous density at both T3 Cu sites, but no anomalous signal was found at either the T1 Cu or the T2 Cu positions. Interestingly, a different magnitude of the anomalous signal was observed when T3 Cu_A and T3 Cu_B were compared in the anomalous difference Fourier map, as can be seen in Fig. 6. Differences in T3 Cu occupancies were also found when

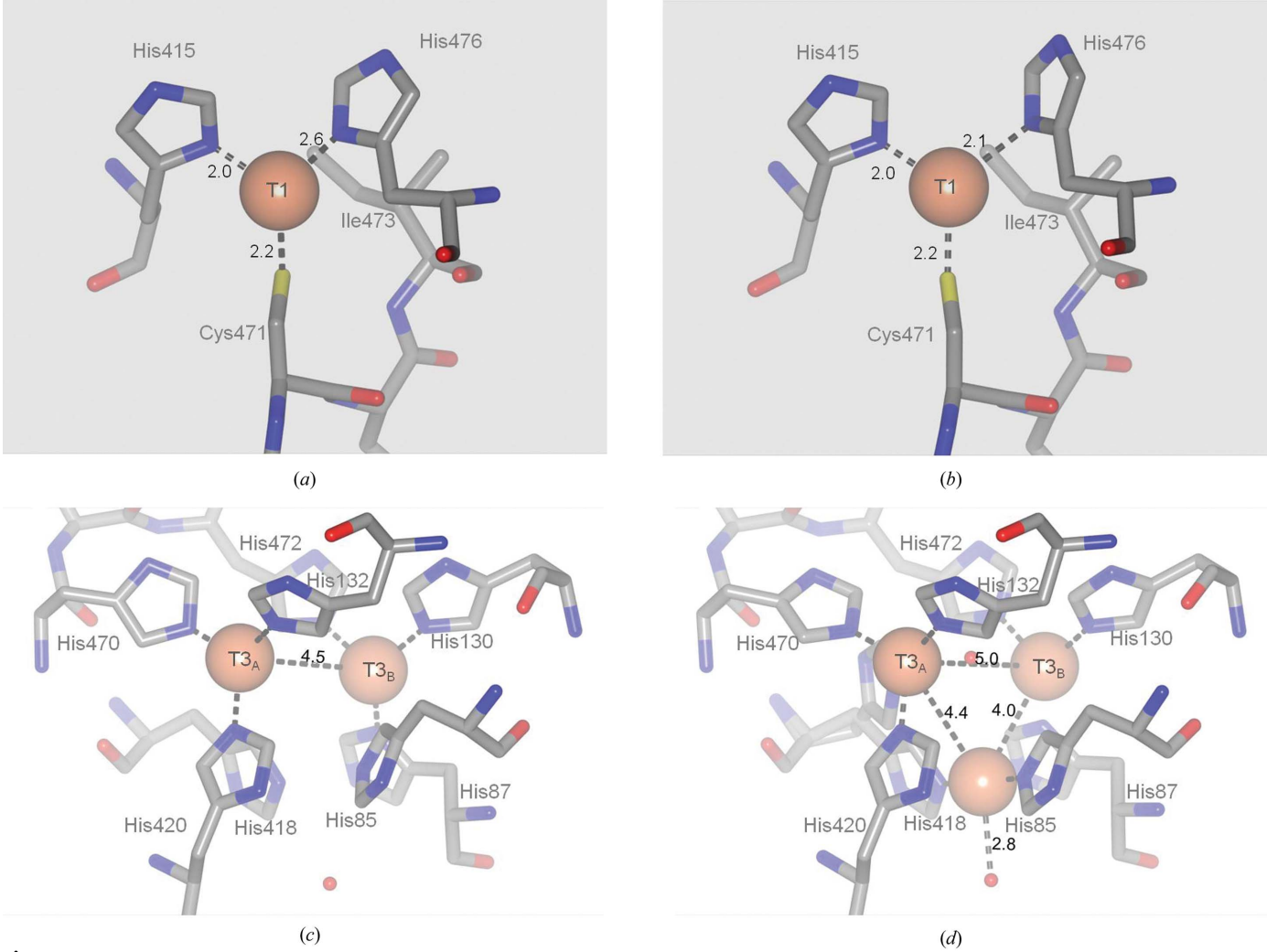

Figure 5
Structural differences observed in Cg L crystals irradiated at different pH values. Differences at T1 Cu are shown in (*a*) and (*b*), and differences observed at the TNC (T2 Cu/T3 Cu) are displayed in (*c*) and (*d*). (*a*, *c*) pH 4.0, (*b*, *d*) pH 5.5.

comparing structures from crystals irradiated in-house and at the synchrotron. An average occupancy of 0.8 was observed for in-house structures (Table 4), while occupancies of around 0.5 were refined for the two structures from crystals exposed at NSLS (not shown), suggesting that at higher absorbed doses T3 Cu ions are more susceptible to radiolysis. The total sum of copper-ion occupancies calculated from crystals exposed at the synchrotron source was lower than 1.5, *i.e.* about one anomalous dispersor per 333 residues; generally, one anomalous dispersor per 100 residues is accepted to be necessary in order to obtain/estimate phases by anomalous methods. This low anomalous dispersor number per number of residues could be one of the reasons why attempts to determine phases derived from the anomalous dispersion of Cu atoms failed.

3.5. X-ray-induced copper reduction

To test whether or not copper reduction occurs during X-ray irradiation, we first demonstrated that solvated electrons are generated in a 30 mg ml^{-1} Cg L solution: the protein was concentrated in a cryosolution identical to that in which crystal diffraction took place. A drop of the protein solution was placed in a cryoloop and mounted on ESRF beamline ID 14-4 at 100 K, where UV–Vis spectra were recorded during X-ray exposure using an online microspectrophotometer (McGeehan *et al.*, 2009). After shutter opening, the appearance of a peak at 590 nm was clearly observable (data not shown). Previously, McGeehan *et al.* (2009) identified such a signal as the formation of solvated electrons.

Independently, X-ray fluorescence (XRF) spectra from Cg L crystals irradiated at 0.9795 Å were collected before and after data collection. For the non-irradiated crystal, a single peak was observed at 8999 eV in the fluorescence spectrum (Fig. 7, continuous line) characteristic of the oxidized state Cu^{II} (Kau *et al.*, 1987). After data collection and an estimated dose of 5.9 MGy, the intensity of the peak at ∼8999 eV decreased and a shoulder appeared at 8987 eV (Fig. 7, dotted line). This shoulder at lower energy is characteristic of the cuprous or reduced form Cu^{I} (Kau *et al.*, 1987). This result confirmed that copper ions in the protein crystal were reduced owing to X-ray irradiation.

To demonstrate that copper reduction does not change the coordination distances at the T1 Cu, the in-house structures were compared with the structure of the crystal from which the oxidized and reduced spectra were collected. As can be seen in Table 4, the coordination distances of T1 Cu from this crystal are practically identical to the prototypical distances for this site. Together with the fluorescence spectra, this result suggests that reduction of the copper centres does not induce changes in coordination distances at the T1 Cu in the models derived from X-ray diffraction.

3.6. X-ray-induced reduction of O_2 intermediates

To identify the intermediates in X-ray-induced O_2 reduction and/or the intermediate occupancies of copper sites, particularly of T1 Cu and T2 Cu, data sets collected at a wavelength of 0.9795 Å from three different crystals grown at pH 7.0 were combined, producing four composite data sets corresponding to increasing absorbed dose levels. As every composite data set consisted of a quarter of a complete data set from a single crystal (16 MGy), the estimated dose during each of the composite data sets was 4 MGy and the four composites thus corresponded to doses of 4, 8, 12 and 16 MGy, respectively.

No electron density was observed for T2 Cu even for the lowest dose composite data set (4 MGy). In combination with results obtained from in-house structures, this observation suggests that in crystals grown at pH 7.0 T2 Cu radiolysis occurs at absorbed doses lower than 4 MGy but higher than 0.62 MGy (the in-house data set). No changes in the electron

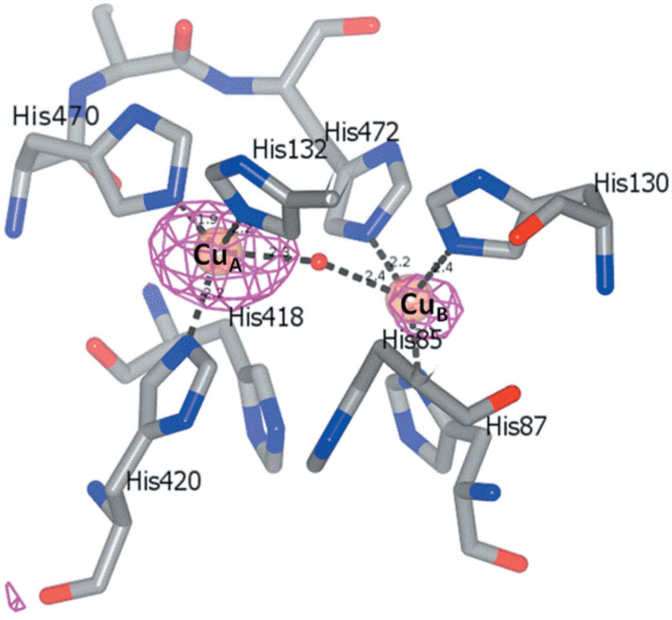

Figure 6
Anomalous map showing asymmetry in the electron density at T3 Cu$_A$ and T3 Cu$_B$. The map (magenta) is contoured at 0.7 e Å^{-3}. Data were obtained at NSLS at an incident wavelength of 1.3778 Å.

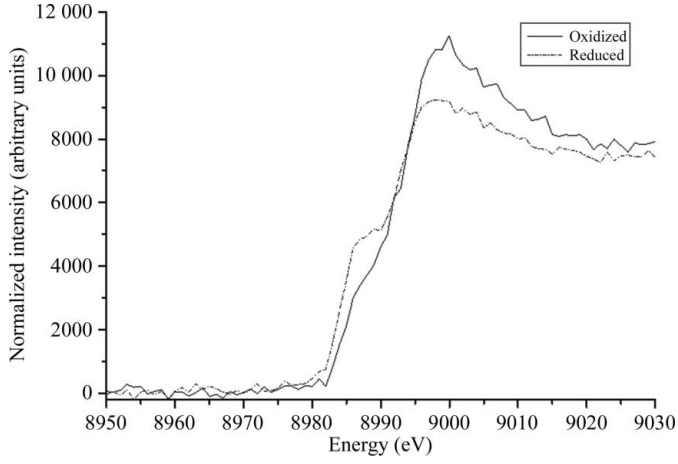

Figure 7
X-ray absorption spectra showing the reduction of Cu^{II} to Cu^{I} upon X-ray irradiation. The oxidized spectrum (solid line) corresponds to Cg L crystals before X-ray data collection, while the reduced spectrum (dotted line) shows that reduction occurs during collection of a complete data set.

density calculated for T1 Cu or T3 Cu in the dose interval examined were revealed by $F_o - F_o$ difference maps (not shown).

3.7. Specific structural damage

We analysed the specific structural damage to protein residues in order to determine whether radiation damage is concentrated at copper centres over the range of absorbed doses tested. No negative densities in an $F_o - F_c$ map at disulfide bridges, methionines or acidic residues were observed in low-dose structures from the data sets collected in-house at pH 4.0, 5.5 or 7.0.

In order to investigate the damage at higher doses, a difference $F_{od1} - F_{od2}$ map was calculated from two sequential data sets collected from the crystal exposed at a wavelength of 0.9795 Å. In this case, positive peaks indicating specific damage were observed at both disulfides: Cys106–Cys506 and Cys138–Cys225 (not shown). No negative peaks were observed at 0.18 e Å^{-3} at the positions of either of the T3 Cu ions. This observation indicates that at doses higher than 4.6 MGy damage does not change occupancy levels of Cu atoms but does produce changes in specific protein residues. Simultaneous with the partial occupancy and the increase in bond lengths observed at pH 4 for the T1 Cu site, an increase by a factor of two in the normalized atomic displacement parameters (ADPs) for α-helix 9 (H9), residues 451–459, was observed when the pH 4.0 and synchrotron-derived structures were compared with the pH 5.5 and 7.0 structures. Interestingly, there are two acidic residues, Asp474 and Glu488, in H9 that have been implicated in catalysis as a proton donor for O_2 reduction and as the E°_{T1} determinant, respectively (Piontek *et al.*, 2002). In mononuclear copper proteins such as azurin and amicyanin the helix corresponding to Cg L H9 has been reported to be involved in redox-potential modulation (Buning *et al.*, 2000; Canters *et al.*, 2000; Remenyi *et al.*, 2001). A theoretical calculation of the pK_a of these acidic residues indicates that only Glu488 is susceptible to protonation in the pH range analyzed in this work [pK_a(Asp452) = 7.5 and pK_a(Glu462) = 4.9 as calculated using the *PROPKA* server; Olsson *et al.*, 2011]. As mentioned above, Asp452 is part of a hydrogen-bonding network inside the O_2-access channel which leads to the TNC, while Glu462 forms a hydrogen bond to Ser118 located in domain 1 of the protein. Two additional acidic residues (Asp98, pK_a = 4.63; Asp444, pK_a = 2.05) that are highly conserved among all BMCOs are located in the water-exit channel. As also mentioned above, Asp98 plays a role in O—O bond breakage by deprotonating the T2 Cu-coordinating water (Quintanar *et al.*, 2005). In contrast to the residues located in H9, no radiation damage or increase in ADPs was observed for these residues.

4. Discussion

4.1. Copper depletion

The copper quantitation and spectroscopic data, together with the sum of the occupancies calculated in all the crystallographic structures determined during this work, indicate that Cg L crystals are subject to X-ray-induced reduction and radiolysis; even when an irradiated Cg L crystal is dissolved no activity is measured, while Cg L from a dissolved non-irradiated crystal is still active. Activity profiles determined in solution over the pH range 2.5–6.0 confirmed that the enzyme was active throughout the pH interval, indicating that inactivation is caused by metal depletion. Additionally, crystals grown at acidic pH retained the capability to oxidize phenolic substrates, as confirmed by the orange colour caused by the appearance of the oxidized DMP product, suggesting the presence of all copper types.

We were unable to isolate structures with intermediate occupancies at the copper sites by forming composite data sets from crystals irradiated at a synchrotron source or by inspection of XAS spectra showing intermediate reduced states at different doses. In agreement with this observation, it has been shown that these radiation-induced processes occur at doses considerably lower than those tested during this work. For example, for ferryl cytochrome *c* peroxidase less than 40% of the unreduced-state population remained after a dose of 0.5 MGy at 65 K (Meharenna *et al.*, 2010), while the influence of radiation on myoglobin (Mb) was observable at as low as 0.0053 MGy (Hersleth & Andersson, 2010). We deduce that radiolysis of copper ions is preceded by radiation-induced reduction and that this compromises the affinity of the copper centres for their coordinating residues.

4.2. pH-induced changes

The UV–visible spectra recorded from Cg L solution samples indicate that no significant electronic modifications have occurred at the T1 Cu (608 nm) or T3 Cu (330 nm) sites as a consequence of pH. This observation is supported by the EPR results, in which the g and $A_{\|}$ parameters corresponding to the T1 Cu remained practically unchanged. However, the two populations observed at acidic pH in the T2 Cu EPR region suggest that the configuration of this site is distorted after acidification of the medium. One possible interpretation of the shifts observed in g parameters and hyperfine splitting ($A_{\|}$) of the T2 Cu signals at pH 4.0 and 5.5 (more remarkably at pH 4.0) is a possible protonation of the OH^- ligand of the T2 Cu, causing a conversion to H_2O. As Quintanar *et al.* (2005) have explained previously, DFT calculations predict large changes in the composition of the ground-state wavefunction of the T2 Cu site upon protonation of the hydroxide ligand, which would be evident as larger shifts in both the g values and the hyperfine couplings in the CW EPR spectra. Similar pH-induced changes in the EPR parameters of copper sites have been described in various copper-containing proteins as a consequence of deprotonation of the T2 Cu-coordinating water molecule and/or conformational changes of the protein molecules (Sakurai *et al.*, 1990; Hwang & Lu, 2004; Sakurai, 2006). Based on the crystallographic structure determined at pH 5.5, we could also interpret these changes in terms of the alternative conformation observed in His418, since the movement of this histidine observed at intermediate pH could

explain the two populations observed in the EPR spectra. We have ruled out the possibility of a partially reduced population because the amount of T2 Cu remained constant in the pH interval tested.

No partial occupancies or changes in coordination distances at the primary electron acceptor T1 Cu have previously been reported in BMCO structures, but similar observations have been described for the reduced T1 Cu site of mononuclear blue copper proteins such as pseudoazurin, plastocyanin and amicyanin. The crystal structure of reduced amicyanin from *Paracoccus denitrificans* at pH 4.4 reveals that His95, which serves as a T1 Cu ligand in the oxidized Cu^{II} form, rotates by 180° about the $C^{\beta}-C^{\gamma}$ bond relative to its position in oxidized amocyanin, thus moving away from the copper-coordination sphere (Zhu *et al.*, 1998). The same is true for the reduced structure of *Alcaligenes faecalis* pseudoazurin, in which a rotation of His81 away from the metal causes the geometry of the copper site to become planar trigonal (Vakoufari *et al.*, 1994). At low pH values (pH 3.8), the fourth ligand of Cu^{I} in poplar plastocyanin is broken, making only van der Waals contact with the imidazole ring of His87, and the metal site is trigonally coordinated by His37, Cys84 and Met92. The trigonal geometry of the Cu atom strongly favours Cu^{I} (Guss *et al.*, 1986). All of these observations suggest a reduced state of the T1 Cu in the Cg L structure determined at pH 4.0. The unaltered conformation of the partial occupied and reduced (as determined by XAS) T1 Cu site in the pH 7.0 structure determined at a synchrotron source supports the observation that the changes in coordination distances are a consequence of both the acidic pH and the reduced state. Together with this observation, the electrochemical determination of the catalytic potential (E_{cat}) of Cg L bound to PGE indicates a significant higher E_{cat} at pH 4.0 (0.74 V) compared with those at either pH 5.5 (0.69 V) or pH 7.0 (<0.68 V) (Fig. 8) as a consequence of alterations in the electronic structure of this copper centre.

The geometry of the TNC in the structure determined at pH 7.0 is consistent with those of most fungal BMCOs deposited in the PDB, in which an OH^{-}/H_2O molecule is bound between T3 Cu and in which the T3 Cu_A–T2 Cu and T3 Cu_B–T2 Cu distances are not equal. However, a wide variety of conformations has been observed for the TNC in crystals from different BMCOs or even in different monomers in the same asymmetric unit. For example, in *Bacillus subtilis* CotA the geometry of the TNC depends on the intermediate of O_2 reduction bound to the TNC. While in the oxygen-bound TNC (PDB entry 2x88; Bento *et al.*, 2010) the T3 Cu_A–T3 Cu_B distance is 4.8 Å, this decreases to 4.0 Å in a more reduced structure in which an OH^{-} is bound to the T3 Cu. A change in the T3 $Cu_{A/B}$–T2 Cu distance is also observed when going from the oxidized to a partially reduced structure: in the O_2-bound structure the T3 Cu_A–T2 Cu and T3 Cu_B–T2 Cu distances are 4.6 Å. These distances are shortened to 3.5 and 4.0 Å, respectively, in the reduced structure. This change upon reduction is consistent with the decrease in the T3 Cu_A–T3 Cu_B distance observed in our pH 4.0 structure when compared with the pH 5.5 structure. This observation supports our hypothesis that the pH 4.0 structure corresponds to a reduced state caused by the effects of X-ray irradiation.

Interestingly, these changes in the bound species and in the geometry of the TNC have also been observed in different monomers in the asymmetric unit of the fungal laccases from *Lentinus tigrinus* (PDB entry 2qt6; Ferraroni *et al.*, 2007) and *Thielavia arenaria* (PDB entry 3pps; Kallio *et al.*, 2011). In the first, an oxidized O_2-bound structure in monomer *B* of the *L. tigrinus* asymmetric unit was observed while two water molecules were modelled in monomer *A*, indicating that a split of O_2 has occurred in one of the monomers. Despite changes in the bound species, no geometry changes occurred in the geometry of the TNC. The crystal structure of *T. arenaria* laccase shows the same asymmetry among monomers in the asymmetric unit; monomer *A* shows an O_2 bound to the T3 Cu but in monomer *D* a water molecule is bound to the T3 Cu. Together with the apparent reduction of the O_2, a decrease in the T3 Cu_A–T3Cu_B (4.8 to 4.6 Å) and T3 Cu_B–T2 Cu (4.2 to 3.7 Å) distances consistent with the shortening observed in CotA mentioned above is observed when going from the oxidized to the reduced structure. All of the evidence cited above suggests that the resting state of laccases differs depending on their source and on their specific properties such as redox potential, pH–activity profile and the pK_a value of the proton donors. The resting state of laccases has been proposed to be a hydroxyl moiety bound to the T3 Cu, as seen in our structure determined at pH 7.0. These hydroxyls are postulated to be the origin of the 330 nm shoulder in the UV–Vis absorption spectra of laccases and more generally in the BMCO family. However, from the structures determined from crystals it is clear that the bound O_2-derived species vary from source to source and even between monomers contained in the same unit cell, even when the 330 nm shoulder is present in the UV–Vis spectrum. In consequence, the structure of the resting state in BMCOs remains unresolved. The experimental evidence from Cg L crystals presented above demonstrates that X-ray radiation causes reduction of the copper centres, leading to an end product that can be different from the starting state. If this is true, the final state of the enzyme would

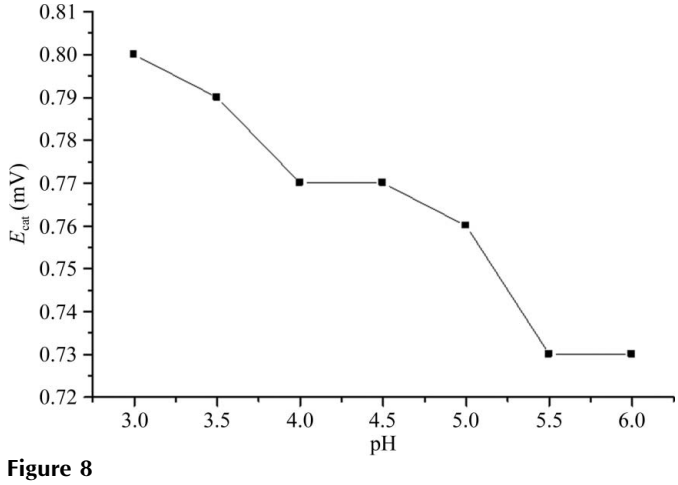

Figure 8
The pH dependence of the catalytic potential (E_{cat}) and its relation to the activity of Cg L is shown.

depend critically on the experimental conditions and the specific susceptibility of each enzyme.

4.3. Intermediate structures and catalytic mechanism

Finally, we interpret the crystallographic structures determined during this work in terms of the O_2-reduction mechanism proposed by Bento *et al.* (2010). In the first step, two electrons are transferred from the T1 Cu to the TNC from a fully functional enzyme in which an O_2 is bound to the T3 Cu site. After the transfer of two electrons the peroxide adduct is formed and the acidic residue closer to the T3 Cu site (Glu498 in CotA and Asp474 in Cg L) is protonated. This change in protonation allows proton donation and transfer of the second two electrons. A native intermediate is then formed containing two hydroxyl groups derived from O_2 splitting. It has recently been demonstrated that protonation of the structurally conserved acidic residue, and consequent proton transfer, is favoured in the reduced state (Iwaki *et al.*, 2010). This latter observation could explain the difference between our in-house determined structures at different pH values: at low pH the coppers are reduced during X-ray exposure and the availability of protons facilitates the reduction of the native state. At higher pH values the availability of protons is limited so that reduction occurs over a larger period of time. Structural rearrangements are needed in order to achieve a configuration that would allow the translocation of one of the hydroxyl groups to the water-exit channel. The Cg L pH 5.5 structure suggests that this rearrangement is favoured by the conformational change of His418, which moves from coordinating the T2 Cu to the T3 Cu_A (Fig. 4). The next step in the mechanism is the protonation of one of the OH^- groups and its consequent release as a water molecule. As the resolution of the Cg L X-ray crystallographic structures determined in this work does not allow us to differentiate between an OH^- ion and a H_2O molecule, we cannot distinguish between this and the last step of the mechanism. An additional protonation of the remaining hydroxyl moiety causes its release as a water molecule and the TNC is ready to accept a new dioxygen molecule, closing the cycle.

All of the above results demonstrate the susceptibility of Cg L copper sites to X-ray-induced reduction and radiolysis. Additionally, a radiolysis order was observed in which the susceptibility of the sites, T2 Cu > T1 Cu > T3 $Cu_B \geq$ T3 Cu_A, could be explained by differential properties of the metal centres, such as the reduction potential of the sites.

EDlM was supported by a PhD fellowship from CONACyT. JEL thanks University College Oxford for a JRF and the Royal Society for a URF. ERP acknowledges financial support from CONACyT project No. 102370 and PAPIIT IN204611. BV thanks CONACyT project No. 128156. The authors thank Biól. Sonia P. Rojas-Trejo for technical assistance and the Ion Beam Centre at the University of Surrey for microPIXE beamtime, as well as Dr Geoff Grime for data-collection assistance. We are also grateful to the staff at the BNL NSLS beamline X6A for data-collection facilities, in particular Dr Vivian Stojanoff and Dr Jean Jakoncic. The X6A beamline is funded by the National Institute of General Medical Sciences, National Institutes of Health under agreement GM-0080. CFB gratefully acknowledges the financial support of the United Kingdom's Engineering and Physical Sciences Research Council (grant No. EP/G00434X/1). The National Synchrotron Light Source, Brookhaven National Laboratory is supported by the US Department of Energy under contract No. DE-AC02-98CH10886. We are grateful to the ESRF for beamtime under Radiation Damage BAG MX-812 and especially to Dr John McGeehan, Dr Antoine Royant, Dr Martin Weik and Dr Andrew McCarthy for valuable assistance with the microspectrophotometry setup. We acknowledge Dr Jeffrey Harmer for his help in the EPR simulation process. We also thank Dr Liliana Quintanar and Dr Lina Rivillas-Acevedo for preliminary EPR experiments and detailed discussions of the manuscript.

References

Adams, P. D. *et al.* (2010). *Acta Cryst.* D**66**, 213–221.
Augustine, A. J., Quintanar, L., Stoj, C. S., Kosman, D. J. & Solomon, E. I. (2007). *J. Am. Chem. Soc.* **129**, 13118–13126.
Benson, D. A., Karsch-Mizrachi, I., Lipman, D. J., Ostell, J. & Sayers, E. W. (2011). *Nucleic Acids Res.* **39**, D32–D37.
Bento, I., Martins, L. O., Lopes, G. G., Carrondo, M. A. & Lindley, P. F. (2005). *Dalton Trans.*, pp. 3507–3513.
Bento, I., Silva, C. S., Chen, Z., Martins, L. O., Lindley, P. F. & Soares, C. M. (2010). *BMC Struct. Biol.* **10**, 28.
Berglund, G. I., Carlsson, G. H., Smith, A. T., Szöke, H., Henriksen, A. & Hajdu, J. (2002). *Nature (London)*, **417**, 463–468.
Bertrand, T., Jolivalt, C., Briozzo, P., Caminade, E., Joly, N., Madzak, C. & Mougin, C. (2002). *Biochemistry*, **41**, 7325–7333.
Blanford, C. F., Heath, R. S. & Armstrong, F. A. (2007). *Chem. Commun.*, pp. 1710–1712.
Bordoli, L., Kiefer, F., Arnold, K., Benkert, P., Battey, J. & Schwede, T. (2009). *Nature Protoc.* **4**, 1–13.
Bradford, M. M. (1976). *Anal. Biochem.* **72**, 248–254.
Buning, C., Canters, G. W., Comba, P., Dennison, C., Jeuken, L., Melter, M. & Sanders-Loehr, J. (2000). *J. Am. Chem. Soc.* **122**, 204–211.
Burmeister, W. P. (2000). *Acta Cryst.* D**56**, 328–341.
Canters, G. W., Kolczak, U., Armstrong, F., Jeuken, L. J., Camba, R. & Sola, M. (2000). *Faraday Discuss.* **115**, 205–220.
Chen, Z., Durão, P., Silva, C. S., Pereira, M. M., Todorovic, S., Hildebrandt, P., Bento, I., Lindley, P. F. & Martins, L. O. (2010). *Dalton Trans.* **39**, 2875–2882.
Cole, J. L., Clark, P. A. & Solomon, E. I. (1990). *J. Am. Chem. Soc.* **112**, 9534–9548.
Cracknell, J. A., Vincent, K. A. & Armstrong, F. A. (2008). *Chem. Rev.* **108**, 2439–2461.
Dos Santos, L., Climent, V., Blanford, C. F. & Armstrong, F. A. (2010). *Phys. Chem. Chem. Phys.* **12**, 13962–13974.
Ducros, V., Brzozowski, A. M., Wilson, K. S., Brown, S. H., Ostergaard, P., Schneider, P., Yaver, D. S., Pedersen, A. H. & Davies, G. J. (1998). *Nature Struct. Biol.* **5**, 310–316.
Ducros, V., Brzozowski, A. M., Wilson, K. S., Østergaard, P., Schneider, P., Svendson, A. & Davies, G. J. (2001). *Acta Cryst.* D**57**, 333–336.
Emsley, P., Lohkamp, B., Scott, W. G. & Cowtan, K. (2010). *Acta Cryst.* D**66**, 486–501.
Enguita, F. J., Marcal, D., Martins, L. O., Grenha, R., Henriques, A. O., Lindley, P. F. & Carrondo, M. A. (2004). *J. Biol. Chem.* **279**, 23472–23476.
Evans, P. (2006). *Acta Cryst.* D**62**, 72–82.

Felsenfeld, G. (1960). *Arch. Biochem. Biophys.* **87**, 247–251.
Ferraroni, M., Myasoedova, N. M., Schmatchenko, V., Leontievsky, A. A., Golovleva, L. A., Scozzafava, A. & Briganti, F. (2007). *BMC Struct. Biol.* **7**, 60.
Fourmond, V., Hoke, K., Heering, H. A., Baffert, C., Leroux, F., Bertrand, P. & Léger, C. (2009). *Bioelectrochemistry*, **76**, 141–147.
Garavaglia, S., Cambria, M. T., Miglio, M., Ragusa, S., Iacobazzi, V., Palmieri, F., D'Ambrosio, C., Scaloni, A. & Rizzi, M. (2004). *J. Mol. Biol.* **342**, 1519–1531.
Garman, E. (1999). *Structure*, **7**, R291–R299.
Garman, E. F. (2010). *Acta Cryst.* D**66**, 339–351.
Garman, E. F. & Grime, G. W. (2005). *Prog. Biophys. Mol. Biol.* **89**, 173–205.
Grime, G. W., Dawson, M., Marsh, M., McArthur, I. C. & Watt, F. (1991). *Nucl. Instrum. Methods Phys. Res. B*, **54**, 52–63.
Guss, J. M., Harrowell, P. R., Murata, M., Norris, V. A. & Freeman, H. C. (1986). *J. Mol. Biol.* **192**, 361–387.
Hakulinen, N., Andberg, M., Kallio, J., Koivula, A., Kruus, K. & Rouvinen, J. (2008). *J. Struct. Biol.* **162**, 29–39.
Hakulinen, N., Kruus, K., Koivula, A. & Rouvinen, J. (2006). *Biochem. Biophys. Res. Commun.* **350**, 929–934.
Hall, J. F., Kanbi, L. D., Strange, R. W. & Hasnain, S. S. (1999). *Biochemistry*, **38**, 12675–12680.
Hanna, P. M., Tamilarasan, R. & McMillin, D. R. (1988). *Biochem. J.* **256**, 1001–1004.
Hersleth, H. P. & Andersson, K. K. (2010). *Biochim. Biophys. Acta*, **1814**, 785–796.
Hwang, H. J. & Lu, Y. (2004). *Proc. Natl Acad. Sci. USA*, **101**, 12842–12847.
Iwaki, M., Kataoka, K., Kajino, T., Sugiyama, R., Morishita, H. & Sakurai, T. (2010). *FEBS Lett.* **584**, 4027–4031.
Johansson, S. A. E., Campbell, J. L. & Malmqvist, K. G. (1995). *Particle-Induced X-ray Emission Spectrometry (PIXE)*. New York: John Wiley & Sons.
Kallio, J. P., Auer, S., Jänis, J., Andberg, M., Kruus, K., Rouvinen, J., Koivula, A. & Hakulinen, N. (2009). *J. Mol. Biol.* **392**, 895–909.
Kallio, J. P., Gasparetti, C., Andberg, M., Boer, H., Koivula, A., Kruus, K., Rouvinen, J. & Hakulinen, N. (2011). *FEBS J.* **278**, 2283–2295.
Kau, L. S., Spira-Solomon, D. J., Penner-Hahn, J. E., Hodgson, K. O. & Solomon, E. I. (1987). *J. Am. Chem. Soc.* **109**, 6433–6442.
Komori, H., Miyazaki, K. & Higuchi, Y. (2009). *FEBS Lett.* **583**, 1189–1195.
Kosman, D. J. (2010). *J. Biol. Inorg. Chem.* **15**, 15–28.
Kunamneni, A., Plou, F. J., Ballesteros, A. & Alcalde, M. (2008). *Recent Pat. Biotechnol.* **2**, 10–24.
Larkin, M. A., Blackshields, G., Brown, N. P., Chenna, R., McGettigan, P. A., McWilliam, H., Valentin, F., Wallace, I. M., Wilm, A., Lopez, R., Thompson, J. D., Gibson, T. J. & Higgins, D. G. (2007). *Bioinformatics*, **23**, 2947–2948.
Laskowski, R. A., MacArthur, M. W., Moss, D. S. & Thornton, J. M. (1993). *J. Appl. Cryst.* **26**, 283–291.
Leslie, A. G. W. (2006). *Acta Cryst.* D**62**, 48–57.
Lewis, N. S. & Nocera, D. G. (2006). *Proc. Natl Acad. Sci. USA*, **103**, 15729–15735.
Lyashenko, A. V. *et al.* (2006). *Acta Cryst.* F**62**, 954–957.
Macedo, S., Pechlaner, M., Schmid, W., Weik, M., Sato, K., Dennison, C. & Djinović-Carugo, K. (2009). *J. Synchrotron Rad.* **16**, 191–204.
Machonkin, T. E., Quintanar, L., Palmer, A. E., Hassett, R., Severance, S., Kosman, D. J. & Solomon, E. I. (2001). *J. Am. Chem. Soc.* **123**, 5507–5517.
Matera, I., Gullotto, A., Tilli, S., Ferraroni, M., Scozzafava, A. & Briganti, F. (2008). *Inorg. Chim. Acta*, **361**, 4129–4137.
McGeehan, J., Ravelli, R. B. G., Murray, J. W., Owen, R. L., Cipriani, F., McSweeney, S., Weik, M. & Garman, E. F. (2009). *J. Synchrotron Rad.* **16**, 163–172.
Meharenna, Y. T., Doukov, T., Li, H., Soltis, S. M. & Poulos, T. L. (2010). *Biochemistry*, **49**, 2984–2986.
Messerschmidt, A., Luecke, H. & Huber, R. (1993). *J. Mol. Biol.* **230**, 997–1014.
Murray, J. W., Garman, E. F. & Ravelli, R. B. G. (2004). *J. Appl. Cryst.* **37**, 513–522.
Murshudov, G. N., Skubák, P., Lebedev, A. A., Pannu, N. S., Steiner, R. A., Nicholls, R. A., Winn, M. D., Long, F. & Vagin, A. A. (2011). *Acta Cryst.* D**67**, 355–367.
Nave, C. & Garman, E. F. (2005). *J. Synchrotron Rad.* **12**, 257–260.
Oliéric, V., Ennifar, E., Meents, A., Fleurant, M., Besnard, C., Pattison, P., Schiltz, M., Schulze-Briese, C. & Dumas, P. (2007). *Acta Cryst.* D**63**, 759–768.
Olsson, M. H. M., Søndergaard, C. R., Rostkowski, M. & Jensen, J. H. (2011). *J. Chem. Theory Comput.* **7**, 525–537.
O'Neill, P., Stevens, D. L. & Garman, E. (2002). *J. Synchrotron Rad.* **9**, 329–332.
Owen, R. L., Holton, J. M., Schulze-Briese, C. & Garman, E. F. (2009). *J. Synchrotron Rad.* **16**, 143–151.
Paithankar, K. S., Owen, R. L. & Garman, E. F. (2009). *J. Synchrotron Rad.* **16**, 152–162.
Paulus, U. A., Wokaun, A., Scherer, G. G., Schmidt, T. J., Stamenkovic, V., Radmilovic, V., Markovic, N. M. & Ross, P. N. (2002). *J. Phys. Chem. B*, **106**, 4181–4191.
Pickard, M. A., Roman, R., Tinoco, R. & Vazquez-Duhalt, R. (1999). *Appl. Environ. Microb.* **65**, 3805–3809.
Piontek, K., Antorini, M. & Choinowski, T. (2002). *J. Biol. Chem.* **277**, 37663–37669.
Polyakov, K. M., Fedorova, T. V., Stepanova, E. V., Cherkashin, E. A., Kurzeev, S. A., Strokopytov, B. V., Lamzin, V. S. & Koroleva, O. V. (2009). *Acta Cryst.* D**65**, 611–617.
Quintanar, L., Stoj, C., Wang, T.-P., Kosman, D. J. & Solomon, E. I. (2005). *Biochemistry*, **44**, 6081–6091.
Ravel, B. & Newville, M. (2005). *J. Synchrotron Rad.* **12**, 537–541.
Ravelli, R. B. G. & Garman, E. F. (2006). Curr. Opin. Struct. Biol. **16**, 624–629.
Ravelli, R. B. G. & McSweeney, S. M. (2000). *Structure*, **8**, 315–328.
Remenyi, R., Jeuken, L. J., Comba, P. & Canters, G. W. (2001). *J. Biol. Inorg. Chem.* **6**, 23–26.
Sakurai, T. (2006). *FEBS Lett.* **580**, 1729–1732.
Sakurai, T., Suzuki, S. & Chikira, M. (1990). *J. Biochem.* **107**, 37–42.
Solomon, E. I., Sundaram, U. M. & Machonkin, T. E. (1996). *Chem. Rev.* **96**, 2563–2606.
Stoll, S. & Schweiger, A. (2006). *J. Magn. Reson.* **178**, 42–55.
Taylor, A. B., Stoj, C. S., Ziegler, L., Kosman, D. J. & Hart, P. J. (2005). *Proc. Natl Acad. Sci. USA*, **102**, 15459–15464.
Tye, J. W., Hall, M. B. & Darensbourg, M. Y. (2005). *Proc. Natl Acad. Sci. USA*, **102**, 16911–16912.
Vagin, A. & Teplyakov, A. (2010). *Acta Cryst.* D**66**, 22–25.
Vaguine, A. A., Richelle, J. & Wodak, S. J. (1999). *Acta Cryst.* D**55**, 191–205.
Vakoufari, E., Wilson, K. S. & Petratos, K. (1994). *FEBS Lett.* **347**, 203–206.
Weik, M., Ravelli, R. B. G., Kryger, G., McSweeney, S., Raves, M. L., Harel, M., Gros, P., Silman, I., Kroon, J. & Sussman, J. L. (2000). *Proc. Natl Acad. Sci. USA*, **97**, 623–628.
Winn, M. D. *et al.* (2011). *Acta Cryst.* D**67**, 235–242.
Zhu, Z., Cunane, L. M., Chen, Z., Durley, R. C., Mathews, F. S. & Davidson, V. L. (1998). *Biochemistry*, **37**, 17128–17136.